crystals

MDPI

Article

Numerical Modeling of Hybrid Solar/Thermal Conversion Efficiency Enhanced by Metamaterial Light Scattering for Ultrathin PbS QDs-STPV Cell

Oussama Baitiche [1], Fathi Bendelala [1], Ali Cheknane [1], Abdelaziz Rabehi [2,3,*] and Elisabetta Comini [2]

[1] Laboratoire Matériaux, Systèmes Énergétiques, Énergies Renouvelables et Gestion de l'Énergie (LMSEERGE), Université Amar Telidji de Laghouat, Bd des Martyrs BP37G, Laghouat 03000, Algeria; o.baitiche@lagh-univ.dz (O.B.); f.bendellala@lagh-univ.dz (F.B.); a.cheknane@lagh-univ.dz (A.C.)
[2] SENSOR Laboratory, University of Brescia, Via D. Valotti 9, 25133 Brescia, Italy; elisabetta.comini@unibs.it
[3] Telecommunications and Smart Systems Laboratory, University of Djelfa, P.O. Box 3117, Djelfa 17000, Algeria
* Correspondence: abdelaziz.rabehi@unibs.it

Abstract: Ultrathin cells are gaining popularity due to their lower weight, reduced cost, and enhanced flexibility. However, compared to bulk cells, light absorption in ultrathin cells is generally much lower. This study presents a numerical simulation of a metamaterial light management structure made of ultrathin lead sulfide colloidal quantum dots (PbS CQDs) sandwiched between a top ITO grating and a tungsten backing to develop an efficient hybrid solar/thermophotovoltaic cell (HSTPVC). The optical properties were computed using both the finite integration technique (FIT) and the finite element method (FEM). The absorptance enhancement was attributed to the excitations of magnetic polaritons (MP), surface plasmon polaritons (SPP), and lossy mode resonance (LMR). The HSTPVC with the metamaterial optical light management structure was assessed for short-circuit current density, open-circuit voltage, and conversion efficiency. The results show a conversion efficiency of 18.02% under AM 1.5 solar illumination and a maximum thermophotovoltaic conversion efficiency of 12.96% at TB = 1600 K. The HSTPVC can operate in a hybrid solar/thermal conversion state when the ITO grating is included by combining the advantages of QDs and metamaterials. This work highlights the potential for developing a new generation of hybrid STPV cells through theoretical modeling and numerical simulations.

Keywords: metamaterial; plasmonics; colloidal quantum dots; hybrid conversion

Citation: Baitiche, O.; Bendelala, F.; Cheknane, A.; Rabehi, A.; Comini, E. Numerical Modeling of Hybrid Solar/Thermal Conversion Efficiency Enhanced by Metamaterial Light Scattering for Ultrathin PbS QDs-STPV Cell. *Crystals* **2024**, *14*, 668. https://doi.org/10.3390/cryst14070668

Academic Editor: Maxim V. Gorkunov

Received: 14 June 2024
Revised: 15 July 2024
Accepted: 17 July 2024
Published: 21 July 2024

1. Introduction

A surface plasmon polariton (SPP) is the most commonly used phenomenon in metamaterials applications, such as absorption, reflection, and scatterings applications, and it can be applied at the metal/dielectric interface by transverse p-polarized light or magnetic fields (TM) [1]. Furthermore, there are two coupling configurations for SPP resonance—Otto and Kretschmann [2]. The Kretschmann configuration is frequently used due to its ease of implementation. Because of its broad range of applications, this field has grown and attracted research attention over many fields, including imaging [3], biosensing [1], and solar energy among other things [4]. Plasmonic materials can be classified into three categories based on the resonances they support. The first category includes plasmonic materials with a real permittivity that is negative and has a greater magnitude than both the imaginary permittivity and the permittivity of the surrounding medium. In the second category, the real part of the permittivity is positive and exceeds both its imaginary permittivity and the permittivity of the surrounding medium [2]. This category of materials exhibits the lossy-mode-resonance (LMR) phenomenon. There is also a third class of materials where the real part of the permittivity is nearly zero, and the imaginary part is significant. Long-range surface exciton-polariton is supported by such a material [5]. Only the first

and second material classes are used in this work. At a certain thickness of the thin film, LMR results from the coupling of the lossy mode and the evanescent wave [6]. Indium tin oxide (ITO) is a type of transparent conducting oxide (TCOs) material that supports both modes of resonances: LMR in the visible range and SPP at infrared region [7]. Electronic and optical properties can be modified during the manufacturing process. LMR excitation offers the benefit of not needing polarization of the incident light [5]. Furthermore, metamaterial light managing plays an essential function in harvesting energy [8], solar cells [9], and thermophotovoltaics [10]. Photovoltaic (PV) and thermophotovoltaic (TPV) technologies convert solar and thermal to electrical power, respectively. Photovoltaic (PV) and thermophotovoltaic (TPV) technologies convert solar and thermal to electrical power, respectively. This technique has three components: a heat source, an emitter, and an appropriate bandgap semiconductor cell [11]. Therefore, many reviews comprehensively studied the first generation of TPV cells [12]. Typically, the TPV and PV cells with a low-bandgap of 0.35 and 1.1 eV usually are limited in terms of efficiency [13]. Most leading candidates for solar/thermal conversion, identified so far as low-bandgap absorber materials, are GaSb (0.73 eV) [14], Ge (0.67 eV) [15], InGaAs (0.36–0.75 eV) [16], GaInAsSb (0.5–0.6 eV) [17], and InAs [18]. Most of these technologies at hand are capable of harnessing only a few portions of the solar/thermal spectrum. Thus, colloidal quantum-dot (CQD) TPVs are attracting researchers owing to their multiple exciton generation (MEG) effects with bandgap tunability and by conceivably breaking the Shockley–Queisser limit [19]. All of these investigations have challenged the optical absorption and forgotten the bulky shape of their architectural design [20]. Semiconducting colloidal quantum dot (CQDs) STPV cells such as lead sulfide (PbS) have sparked much interest in hybrid (thermal/solar) cells because of their low cost, solution-processability, ease of synthesis, and bandgap tunability with MEG properties, as well as their broad absorption spectrum [21]. Because 50% of the sun's energy is found beyond 750 nm, converting critical infrared photons is an important feature that CQDs can provide. The most widely investigated cells for this semiconductor are based on depleted bulk heterojunctions formed by CQD layer deposition on top of an electron-accepting layer like ZnO. Increasing the STPV cell's light absorption is essential to raising its power conversion efficiency. Increasing the thickness of the active layer is not the best approach for efficiency gains. PbS QDs have a typical minority carrier diffusion length between 200 and 300 nm, which roughly defines the maximum active layer thickness for optimal performance [22]. As a consequence, increasing the cell thickness to about 3 μm to absorb all infrared incident photons is not feasible. Improving efficiency requires a two-pronged approach: maximizing light absorption and accounting for carrier transport limitations [23]. Thin-film STPV cells are an alternative solution, and research has been conducted on ultrathin TPV cells to reduce weight, costs, and improve flexibility [24]. The primary problem with thin STPV cells is still ineffective light absorption [25]. A light-trapping strategy is frequently solicited to boost light absorption in thin film cells [26]. Several studies explore the plasmonic effect on STPV cell performance. However, no previous research has combined LMR and plasmonic resonance for a narrow-band gap CQDs ultrathin design, which could be used for hybrid STPV cells [27].

The current study aims to increase the conversion efficiency of STPV cells through a light-trapping-based metamaterial structure that integrates plasmonic and lossy mode resonance (LMR) mechanisms. Illustrated in Figure 1, the proposed hybrid solar/thermophotovoltaic cell (HSTPVC) incorporates an ultrathin colloidal quantum dot (CQD) active layer optimized for hybrid thermal/solar power conversion. The dual functionality of the front ITO grating and rear tungsten film includes light confinement via LMR and surface plasmon polariton (SPP) modes, in addition to serving as electrodes. The narrow bandgap (0.7 eV) of the PbS CQD layer positions it ideally as the active layer. Numerical simulations performed using CST Microwave Studio software 2019 model the optical performance of the proposed design utilizing the finite integration technique (FIT). The analysis involves plotting electromagnetic power densities to clarify the mechanisms enhancing absorptance, complemented by validation through the finite element method (FEM). The study culminates in

an assessment of the electrical performance of the HSTPVC, encompassing evaluations of short-circuit current, open-circuit voltage, and overall conversion efficiency. This rigorous approach provides a comprehensive theoretical analysis of the potential performance of the HSTPV cell under investigation. Moving forward, future research will concentrate on enhancing both the optical and electrical performance of PbS QD cells, potentially involving experimental validation by collaborating with other laboratories to corroborate our findings.

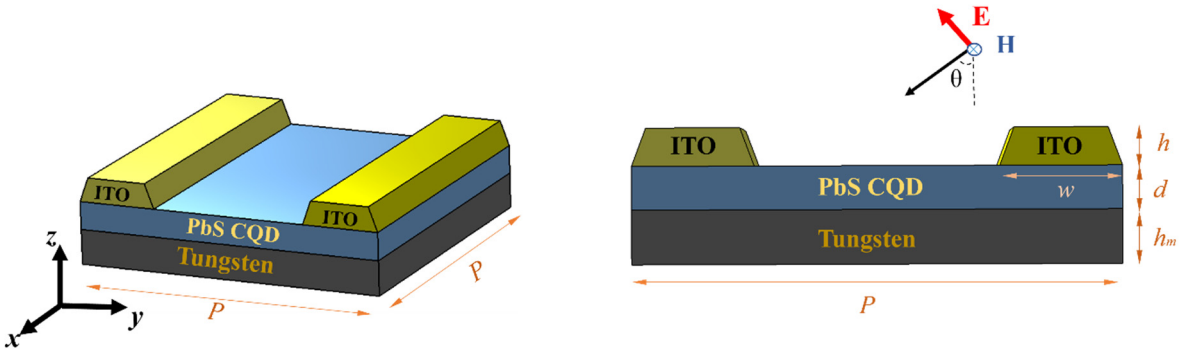

Figure 1. The proposed HSTPVC design. ITO grating size is (h = 120 nm, and w = 200 nm), active layer thickness d = 40 nm, and W metallic film thickness h_m = 100 nm. The unit cell periodicity is P = 900 nm.

2. Materials and Methods

2.1. Numerical Method

The finite integration technique (FIT) has been applied, which was initially proposed by T. Weiland, to solve Maxwell's equations represented by the structure [28]. Thus, the radiation elements of the structure and the density distribution of each part of the electromagnetic field can be determined. In this analysis, all materials have permeabilities (μ = 1). Figure 1 shows the suggested structure of HSTPVC design under study. Parameters are acquired by adjusting the thickness of each layer and the widths of the upper and lower bases of the trapezoidal lattices, and the HSTPVC periodically lies on the plane x-y of an opaque W bottom layer, which comprises two ITO trapezoidal gratings and a planar PbS CQD active spacer. Tungsten is selected as the back layer because of its outstanding high-temperature stability [29]. We test the approach's validity by comparing the estimated absorptions of the suggested HSTPVC to those of a rival method that uses different types of mesh. Both strategies work together to provide more stable and accurate simulations [29].

2.2. Geometric Design

The suggested HSTPVC under study is based on a period of two trapezoidal grating of indium tin oxide (ITO) deposited on a planar CQD lead sulfide (PbS) thin film over a Tungsten (W) back layer of thickness $h_m = 100$ nm as presented in Figure 1. The ITO grating height is $h = 120$ nm with a width $w = 200$ nm extending along the x-direction, where the dielectric properties of ITO are depicted from References [30,31]. The active layer of CQD-PbS has a bandgap of $E_g = 0.7$ eV [32–34], and a thickness of $d = 40$ nm. The unit cell periodicity is chosen to be $P = 900$ nm in both x and y-direction.

The rigorous FIT approach helps compute the electromagnetic characteristics of nanostructured devices [35]. A Floquet's boundary condition for solving a periodic-differential equation expanded by Bloch waves has been applied. The Drude model gives the dielectric function of metallic materials [29]:

$$\varepsilon_M = \varepsilon_\infty - \frac{\omega_p^2}{\omega^2 + i\omega\Gamma} \quad (1)$$

where $\varepsilon_\infty = 1$, $\varepsilon_\infty = 3.95$ the dielectric constants, and $\omega_p(W) = 1445.95$ THz. $\omega_p(ITO) = 461$ THz represents the plasma frequencies for W and ITO, respectively, and Γ_W = 12.08 THz and Γ_{ITO} = 26.59 THz represent the damping coefficient at room temperature for Tungsten and ITO [36]. ITO grating has significant reflectivity qualities in the infrared regime but is transparent in the visible region, making it an excellent option for hybrid conversion [37].

The designed structure's total absorption (α) is computed using [29]:

$$\alpha = 1 - R - T \quad (2)$$

where R is the total reflectance and T is the transmittance. Tungsten film acts as a mirror to the incident waves. Therefore, the transmission is neglected (T = 0), and the absorption is expressed as $\alpha = 1 - R$ [37]. The absorptance is numerically computed under the incoming wave's transverse electric (TE) and transverse magnetic (TM) polarization.

3. Results and Discussion

3.1. Absorbed Energy

Figure 2 illustrates the absorbed energy of the proposed HSTPVC design, computed using the rigorous FIT approach and confirmed by the FEM method under normal incident waves for both TE and TM polarization modes in the visible and infrared (IR) ranges. Both methods show good agreement overall, with a slightly lower but still satisfactory agreement in the short-wave infrared range (SWIR, λ > 1 μm) [38]. For TE polarization (Figure 2a), the absorption spectra show notable similarities between FIT and FEM across the wavelength range of 0.5 to 3 μm. Both methods capture the peaks and troughs of the absorption spectrum, indicating good agreement in their prediction of resonance features. However, differences are observed in the magnitude of absorption at specific wavelengths, particularly around 1.5 μm and 2.2 μm, where FEM exhibits slightly higher absorption values compared to FIT. This result can be intuitively explained by the fact that both solvers require conformal meshing; a defective mesh can introduce significant numerical noise, and both FIT and FEM methods can be built with a specific meshing type, which is hexahedral or tetrahedral, respectively. This confirms that the numerical noises associated with the specific mesh type remain and appear at a particular threshold throughout the simulation. The most popular technique is to employ mesh override zones to compel a tiny spatial mesh near interfaces. The disadvantage of this strategy is that it significantly increases simulation times and memory requirements [38]. Furthermore, under TE polarization, where the electric field is parallel to the grating, only the tangential and normal components of the magnetic field fluctuate with the incoming wave because the magnetic field has a weaker interaction with matter than the electric field [39]. For TM polarization (Figure 2b), the agreement between FIT and FEM is even more pronounced. Both methods display nearly identical absorption spectra from 0.5 to 3 μm, demonstrating a high level of consistency in capturing the optical properties of the HSTPVC for TM polarization. The peaks and troughs align closely, with minimal differences in magnitude and wavelength positions. This suggests that both methods are reliable for simulating the optical behavior under TM polarization [40,41].

The blue region presents the effective photon region higher than the PbS CQD bandgap. It is marked that four significant absorptance peaks (α = 0.88 at λ = 1 μm, α = 0.98 at λ = 0.58 μm, α = 0.96 at λ = 0.45 μm, and α = 0.96 at λ = 0.41 μm) exist under TM mode incoming waves, while there are five major absorptance peaks (α = 0.72 at λ = 1.6 μm, α = 0.87 at λ = 1.00 μm, α = 0.85 at λ = 0.6 μm, α = 0.95 at λ = 0.45 μm, and α = 0.98 at λ = 0.35 μm) under TE incoming mode wave. All the absorptance peaks occur over the bandgap of the active layer and therefore could directly improve the light absorptance for photon-generated carriers. Understanding the physical principles responsible for increased light absorption in the HSTPVC structure is critical. All the absorptance peaks are above the bandgap of the PbS CQD layer and thus could effectively improve the light energy absorptance for photon-generated carriers.

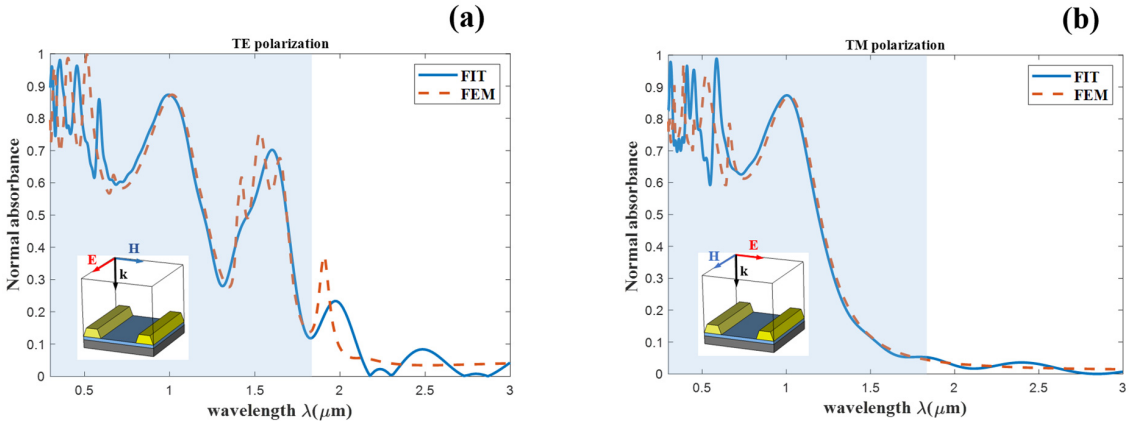

Figure 2. Absorbed energy spectra of the HSTPVC for (**a**) TE and (**b**) TM modes of polarization.

3.2. Absorbed Power per Material

Figure 3a evaluates the normalized absorptance of three arrangements under TM and TE polarization modes: the ITO-PbS QDs-W (entire structure), PbS CQD-W, and the free-standing PbS CQD layer. The active layer thickness in all three configurations is 40 nm. It is found that without the upper ITO strip, the absorptance peak for the TM and TE modes of polarizations at (λ = 0.58 μm, λ = 0.45 μm, and λ = 0.41 μm), as well as at (λ = 1.6 μm, λ = 0.6 μm, λ = 0.45 μm, and λ = 0.35 μm), respectively, disappear. The peak at λ = 1 μm remains but shifts slightly. For a bare active layer, there is a single peak of 0.98 at a wavelength of λ = 0.7 μm to the bandgap due to the smallish intrinsic absorptance coefficient of the PbS CQDs layer.

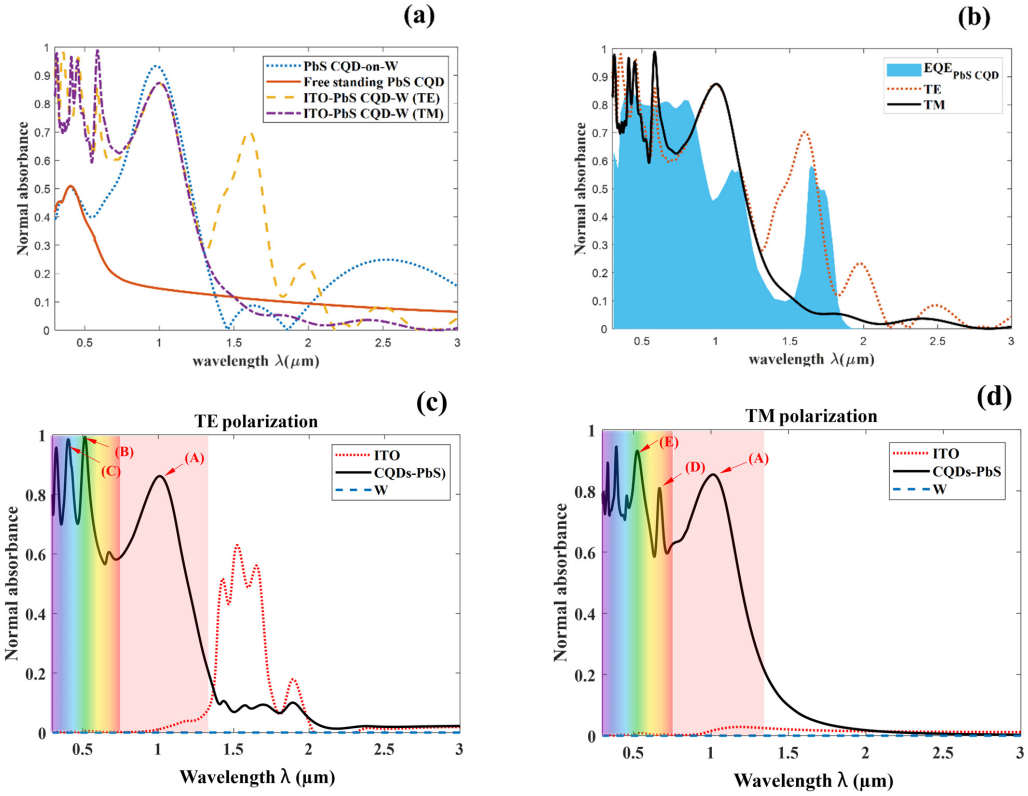

Figure 3. (**a**) Normalized absorptance of three configurations: PbS CQD-on-W, the free-standing active layer (PbS CQD), and the entire structure under TE and TM modes of polarization. (**b**) Normale absorptance of HSTPVC compared to EQE of the active layer and the absorbed energy per material in the suggested HSTPVC under (**c**) TM; (**d**) TE modes of polarization.

Although the absorptance can be notably improved in the HSTPVC structure by exciting MP, SPP, and LMR under a normal incoming wave, the useful photon for the cell (zone in blue) can be represented by the external quantum efficiency (EQE) of the active layer, and the adequate absorption can display a straight contribution to the photon-generated carriers as depicted in Figure 3b. Furthermore, the light absorbed by metals might be considered a leakage power. Hence, it is necessary to assess the amount of power absorbed by the active layer instead of by the whole cell. The entire design can be segmented into three layers: the first layer is the ITO grating, the second is the PbS CQD layer, and the third is the Tungsten layer. The formula for calculating the energy absorbed by the entire design per unit volume within each layer is [25]:

$$P_{abs} = \frac{1}{2}\varepsilon_0 \varepsilon_i'' \omega |E_i|^2 \tag{3}$$

The absorbed energy per layer can be normalized to the incident energy [25]:

$$\alpha_i = \frac{\int P_i dV_i}{0.5 c_0 \varepsilon_0 |E_{inc}|^2 A} \tag{4}$$

where ε_i'' represents the imaginary part of the relative permittivity of the layer, V_i is the volume of layer (i), A is the area exposed to the light source, E_i is the electric field inside layer (i), and E_{inc} is the incoming electric field. The total absorbed energy is the summation of the power absorbed by each layer. Figure 3c,d represent the normalized power absorptance in the PbS CQD layer, the ITO strip, the W film, and the whole structure. It can be observed that the majority power is absorbed by the PbS CQD active layer, while some significant power that exists between 1.4 μm and 2 μm is absorbed by ITO under TE polarization, as shown in Figure 3c. According to Figure 3c,d, HSTPVC has functioned as a thermal converter in the infrared region (zone in red) while also being effective as a solar cell converter in the visible zone. The combination of QD tunability and good absorption demonstrated by the plasmonic's metamaterials allows for the acquisition of a device working under hybrid conditions (thermal/solar conversion).

To help clarify the underlying mechanism for the absorptance peaks, Figure 4 illustrates the amplitude of magnetic field $|H|$'s distribution in the x-z cross-section inside the HSTPVC structure at the peaks: A(λ = 1 μm), B(λ = 0.52 μm), C(λ = 0.40 μm), D(λ = 0.65 μm), and E(λ = 0.52 μm). The absorptance peak at (A, B, D, and E) for the proposed HSTPVC under TM waves is ascribed to the excitation of SPP at the PbS CQD-W interface, as shown in Figure 4a,b,d. SPP waves describe the interchange between EM and the oscillatory behavior of free charges in the interface metal/dielectric when the real component of the metal permittivity is negative and more significant than the real part of the active layer's permittivity [42]. At the same time, the LMR mechanism emerges when the real part of the PbS CQD layer's permittivity is positive and exceeds in magnitude, both in its own imaginary part and the real part of the ITO strip's permittivity as depicted in Figure 4b,c,e [42]. The resonance peak (B) is ascribed to the excitation of magnetic polariton modes (MP). It is evident that the H field creates a current loop between the two trapezoidal ITO gratings and exhibits light solid confinement in the PbS CQD layer. These are the basic properties of MP resonance, as previously stated [25,43].

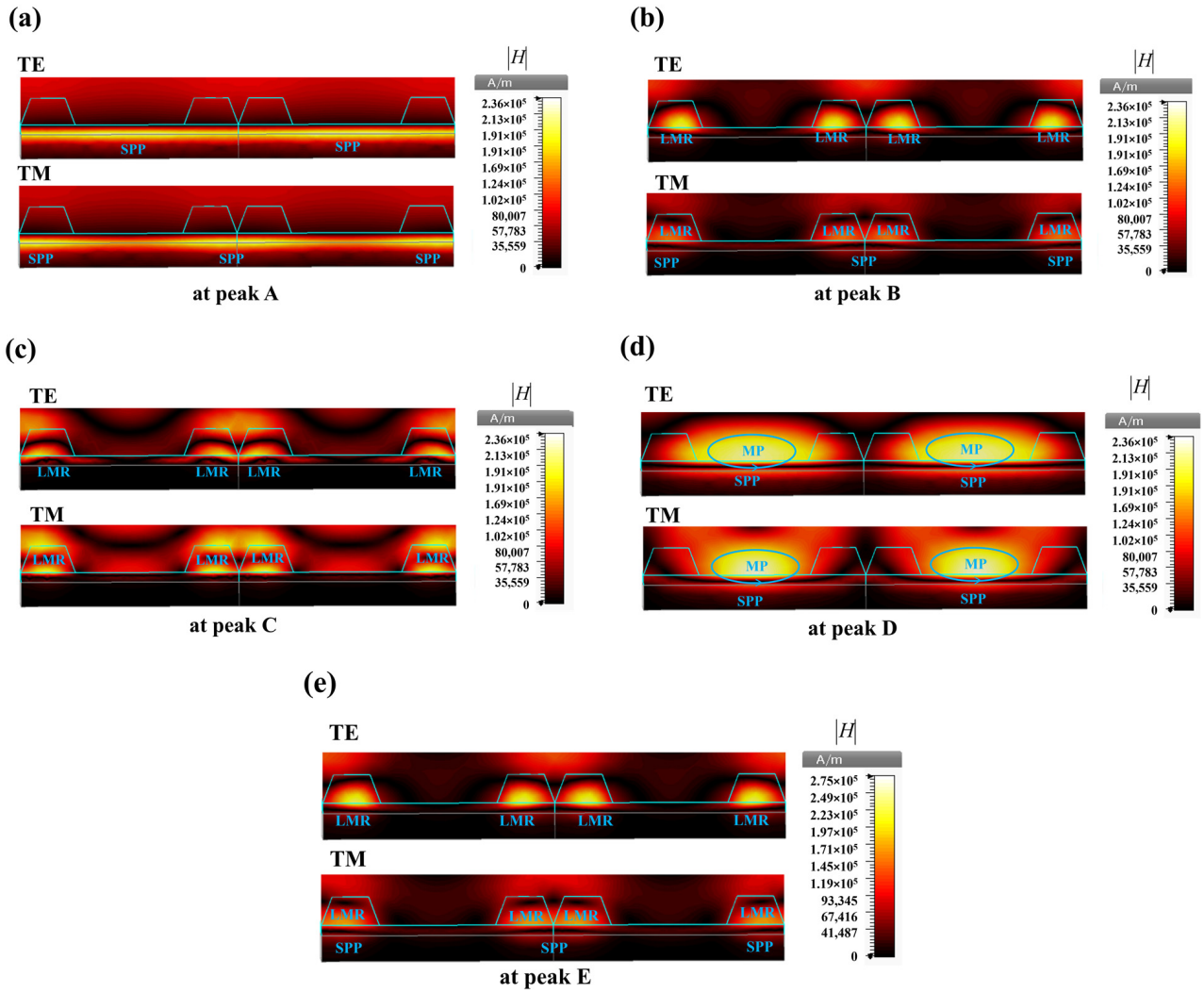

Figure 4. Magnetic field |H| distribution at absorptance peaks: (**a**) A(λ = 1 μm), (**b**) B(λ = 0.52 μm), (**c**) C(λ = 0.40 μm), (**d**) D(λ = 0.65 μm), and (**e**) E(λ = 0.52 μm) for the suggested HSTPVC under TE and TM polarizations.

3.3. SPP, MP, and LMR Behaviors at Oblique Incidence

To further explain the behaviors of MP, SPP, and LMR at an oblique angle of incidences, colormaps of HSTPVC absorptance varying with both wavelength and incident angle (θ) were displayed for TM and TE incident waves in Figure 5. The device operates via two hybrid modes of functionality, photovoltaic (PV) under solar source illumination and thermophotovoltaic (TPV) under blackbody radiation at both TM and TE polarization.

The SPP peaks represent the major absorption mechanism for the TPV mode, which propagates along the (W/PbS CQDs) interface. The static MP modes are observable in the air and PbS layer between the two neighboring ITO grating at wavelengths lower than the plasma frequency of ITO material. Because of active layer, the SPP waves can be easily coupled with MP and LMR modes during the photovoltaic conversion. LMR modes emerge when the real part of ITO's dielectric function turns positive [6].

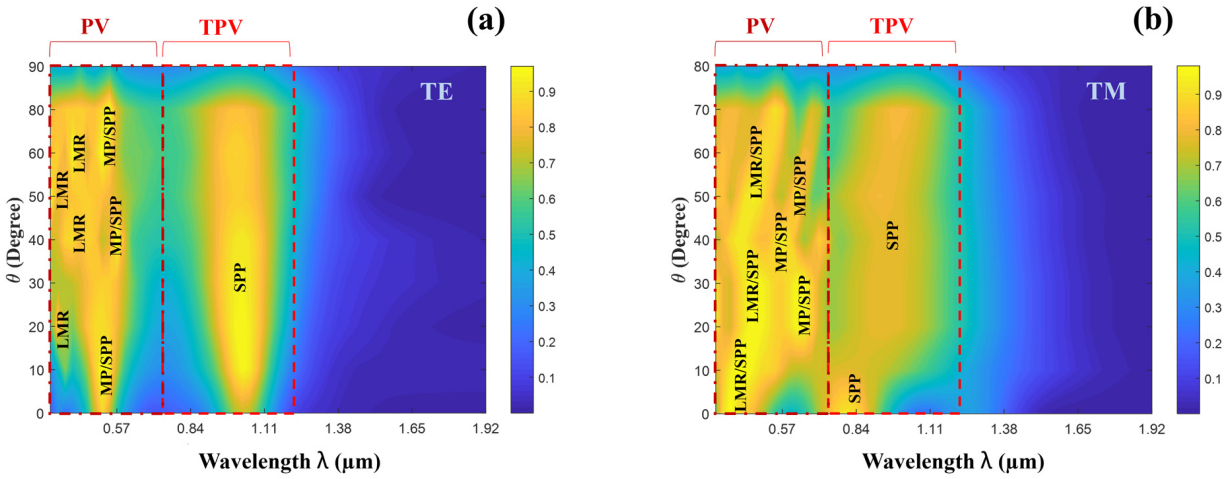

Figure 5. A colormap of the spectral-directional absorptance of the ultrathin HTPVC varying with wavelength and angle of incidence of (**a**) TE modes and (**b**) TM modes.

3.4. Electrical Performance of HSTPVC

To quantify the performance of the suggested HSTPVC as a conversion device, open-circuit voltage, short-circuit current density, output electrical power, and cell conversion efficiency were computed. The short-circuit current J_{sc} (mA/cm^2) density is calculated by [44]:

$$J_{sc} = \int_0^{\frac{hc_0}{E_g}} \frac{q\lambda}{hc_0} \alpha(\lambda)\eta_i(\lambda)E_{b\lambda}(\lambda)d\lambda \tag{5}$$

η_i is the quantum efficiency (QE), $h = 6.225 \times 10^{-34}$ is the Planck's constant, $q = 1.9 \times 10^{-19}$ C is the electron charge, $c_0 = 3 \times 10^8$ m/s is the light velocity in a vacuum, and $E_g = 0.7$ eV is the energy bandgap of PbS CQD cell. The radiative heat flux ($E_{b\lambda}(T)$) defined by Planck's formula as follows [44]:

$$E_{b\lambda}(T) = \frac{C_1}{\lambda^5[\exp(C_2/\lambda T) - 1]} \tag{6}$$

where $C_1 = 3.742 \times 10^8$ W·μm^4/m^2, $C_2 = 1.439 \times 10^4$ μm·K, and T is the blackbody temperature. The total incident radiative flux onto the cell P_{in} (W/cm^2) can be calculated by:

$$P_{in} = \int_0^{\infty} E_{b\lambda}(T)\varepsilon_\lambda d\lambda \tag{7}$$

Here, ε_λ is the spectral emissivity of a diffuse TPV emitter. The open circuit formula is given by [1]

$$V_{oc} = \left(\frac{k_B T_c}{q}\right) \ln\left(\frac{J_{sc}}{J_0} + 1\right) \tag{8}$$

where T_c is the cell temperature, which is taken as 300 K, k_B is the Boltzmann constant, and $J_0 = 1.17 \times 10^{-4}$ mA cm^{-2} is the dark current [2].

The output electric power P_{cell} can be evaluated by involving short current density Equation (5) and open-circuit voltage calculated by [3]:

$$P_{cell} = J_{sc}V_{oc}\left(1 - \frac{1}{y}\right)\left(1 - \frac{\ln(y)}{y}\right) \tag{9}$$

where

$$y = \ln\left(\frac{J_{sc}}{J_0}\right) \tag{10}$$

The overall efficiency of the HSTPVC, which is characterized as the ratio of electric output power over the heat radiated power, can be computed using the following formula:

$$\eta_{cell} = \frac{P_{cell}}{P_{in}} \tag{11}$$

The first stage in optoelectronic devices is to propagate and absorb light in QDs materials. CQD cells typically have operational thicknesses of less than 300 nm [45]. Consequently, it is not possible to just keep thickening the cell to absorb all those IR photons. Changing intrinsic characteristics can also boost the overall absorption of a QD active layer [46]. Increased light absorption in a solar cell often triggers an enhancement in total electrical current and consequently power conversion. Tong et al. estimate that the ultrathin cell's QE is 100% since bulk recombination losses for minority carriers are greatly decreased, and surface recombination losses can be substantially decreased with a strong passivation layer [47]. Figure 6a depicts the spectrum distribution of radiation flux from a blackbody emitter at temperatures ranging from 600 K to 1600 K, as well as the spectral emittance of an ideal selective TPV emitter, which has unity emissivity within the wavelength range from λ_1 to λ_2 and zero emissivity outside this range. The purpose of selective emitters is to prevent the loss of photons with energy ($E_{ph} < E_g$), which cannot generate electron-hole pairs, and to minimize excess energy above the bandgap and thermally isolate the cell, therefore increasing thermal conversion efficiency. Figure 6b shows the short-circuit current and conversion efficiency of the PbS CQD under blackbody radiation at various temperatures. Clearly, the short-circuit current (J_{sc}) may be significantly increased with the ITO-coupled structure, which increases with blackbody temperature. For example, at 1600 K, the short-circuit current of the HTPVC with an ITO-PbS CQD-W configuration is 0.6 mA/cm^2, which is more than twice that of a bare configuration (PbS CQD-W), which corresponds to the TPV conversion rate of 12.67%. Increasing the temperature leads to higher J_{sc}, V_{oc}, and cell efficiency in TPV systems. Higher emittance bandwidth (lower L1) results in high TPV conversion efficiency. A selective emitter is necessary for high efficiency, requiring a specific emittance band and high temperature.

The J_{sc} and (V_{oc}) of HTPVC were displayed as a function of λ_1 and blackbody temperature (see Figure 6c–e). It is clear that the emitter bandwidth has a substantial impact on cell performance. The short-circuit current reduces as the bandwidth decreases (i.e., λ_1 increases), whereas open-circuit voltage varies little, even at the most significant source temperatures. As the bandwidth reduces, the input power (P_{in}) declines faster, resulting in a decrease in generated power (P_{cell}) and conversion efficiency rate (η). With a selective emitter, the highest cell TPV efficiency can be attained as Nmax = 12.67% when λ_1 is approximately 0.3 µm, which is related to the MP, SPP, and LMR absorption process.

It is important to evaluate the potential of this HTPVC device as a hybrid conversion cell to harvest both AM1.5 solar and various blackbody sources in combination with another established similar bandgap cell (E_g = 0.7 eV). The summary of the performance comparison is presented in Table 1, which compares the parameters of the proposed HTPVC to similar hybrid solar cells with low-bandgap (Eg = 0.7 eV) STPV cells in terms of J_{sc}, V_{oc}, FF, and conversion efficiency. The computations were conducted with λ_1 = 0.3 µm and under various power sources: blackbody (T = 1300 K) and solar irradiation (AM 1.5). Combining metamaterial actions (SPP, LMR, and MP) can boost the short-circuit current by increasing the photon absorptance rate across a broadband spectrum, directly impacting cell efficiency. Yu et al. [32] reported a TPV efficiency of 5.9% at a blackbody temperature of 1300 K, whereas our proposed cell demonstrated an efficiency of 10.9% under the same irradiation. Moreover, our HTPVC has an ultrathin active layer (40 nm), which reduces the active layer by 89.61% compared to Yu's cell. Moreover, J_{sc} = 40 mA/cm^2, V_{oc} = 0.49 V, FF = 89%, and efficiency η = 18.08% under AM1.5; these values are three times greater than in Reference [32]. However, in a new study, Chao et al. used a thick PbS active lattice with organic films of PMMA:PCBM to reach a maximum conversion efficiency of η = 15.45% [48].

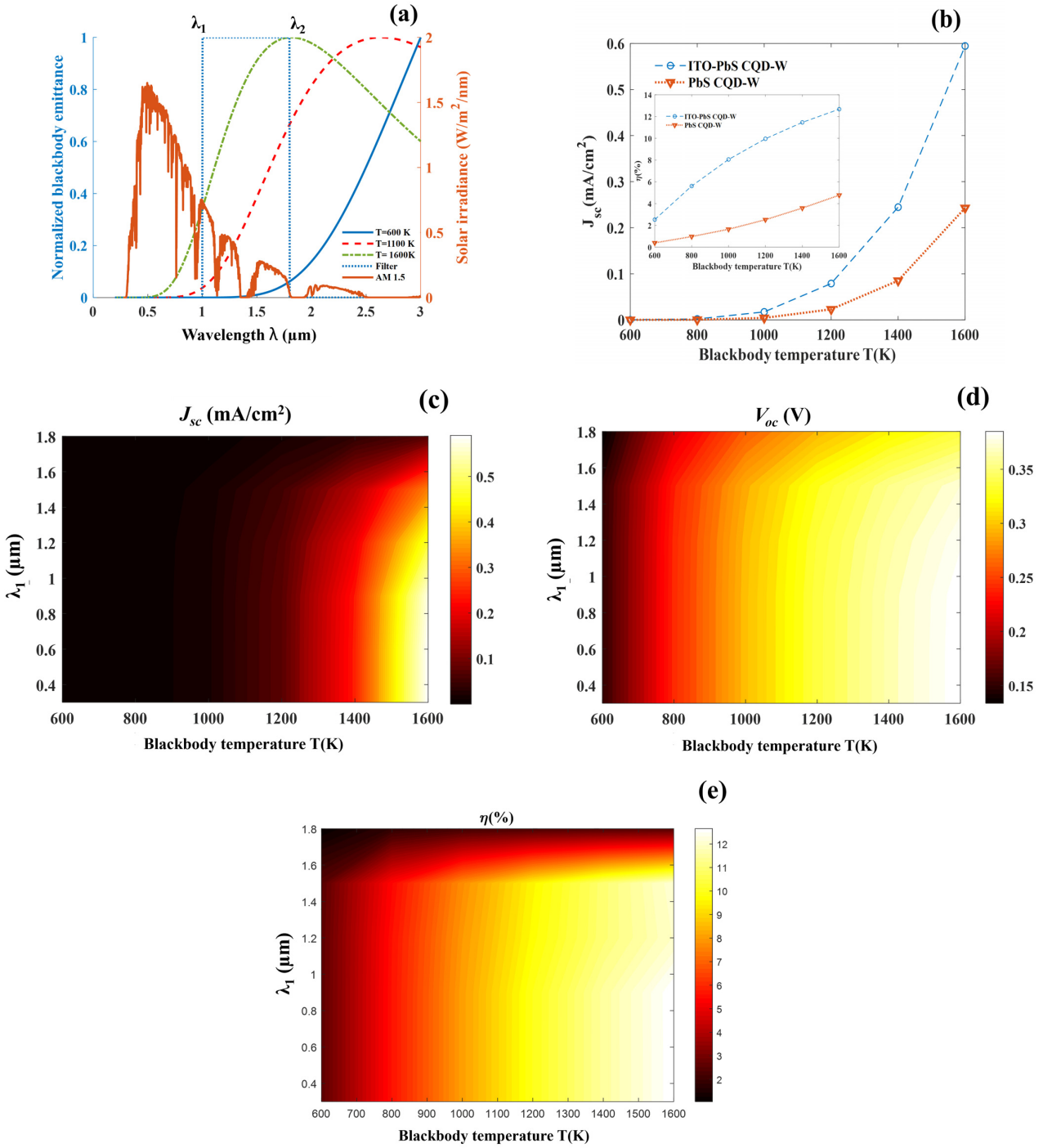

Figure 6. (**a**) Spectral distribution for power fluxes from different power sources with a spectral-ideal filter for a TPV conversion, (**b**) effect of blackbody temperature on J_{sc} (outer graph), and η (inner graph) effect of both blackbody temperature and λ_1 on (**c**) J_{sc}, (**d**) V_{oc}, and (**e**) conversion efficiency (η).

Table 1. A brief comparison of PV and TPV performance summary under AM1.5G solar and thermal source radiation, respectively.

Power Sources	J_{sc} (mA/cm^2)		V_{oc} (V)		FF (%)		η (%)	
	Our Work	[32]	Our Work	[32]	Our Work	[32]	Our Work	[32]
(T = 1300 K)	0.24	0.16	0.36	0.27	64	55	10.9	5.9
AM 1.5	40	37.01	0.49	0.31	89	56	18.02	6.39

4. Conclusions

We have numerically proved that light management of a metamaterial structure can significantly improve the absorptance of visible and IR photons in an ultrathin PbS CQs active layer. The underlying process for the absorptance peaks above the bandgap is revealed to be the excitation of MP, SPP, and LMR, which is explained using the electromagnetic field distribution. With the metamaterial structure, the short-circuit current in the HSTPVC is greatly enhanced and can achieve 40 mA/cm^2 and 0.59 mA/cm^2, and the conversion efficiency can be further increased up to 18% and 12.96% under AM 1.5 and blackbody radiation (T = 1600 K), respectively. The findings and insights gathered here will aid in the creation of next-generation, low-cost, high-efficiency ultrathin hybrid solar/thermal cells.

Author Contributions: Conceptualization, O.B., A.R. and E.C.; data curation, F.B.; funding acquisition, E.C.; investigation, F.B.; methodology, O.B., F.B. and A.C.; project administration, A.C.; resources, A.R. and E.C.; software, O.B.; supervision, F.B. and A.C.; visualization, F.B. and A.R.; writing—original draft, O.B.; writing—review and editing, F.B., A.C., A.R. and E.C. All authors have read and agreed to the published version of the manuscript.

Funding: This research received no external funding.

Data Availability Statement: Data for this research are available upon request, due to privacy.

Conflicts of Interest: The authors declare no conflicts of interest.

References

1. Gupta, B.D.; Sharma, A.K.; Li, J. *Plasmonics-Based Optical Sensors and Detectors*; Jenny Stanford Publishing: New York, NY, USA, 2023. [CrossRef]
2. Maier, S.A. *Plasmonics: Fundamentals and Applications*; Springer: New York, NY, USA, 2007. [CrossRef]
3. Lin, J.-S.; Tian, X.-D.; Li, G.; Zhang, F.-L.; Wang, Y.; Li, J.-F. Advanced plasmonic technologies for multi-scale biomedical imaging. *Chem. Soc. Rev.* **2022**, *51*, 9445–9468. [CrossRef] [PubMed]
4. Shaghouli, E.; Granpayeh, N.; Manavizadeh, N. Plasmonic enhanced ultra-thin solar cell: A combined approach using fractal and nano-antenna structure to maximize absorption. *Results Phys.* **2023**, *50*, 106600. [CrossRef]
5. Gaur, D.S.; Purohit, A.; Mishra, S.K.; Mishra, A.K. An Interplay between Lossy Mode Resonance and Surface Plasmon Resonance and Their Sensing Applications. *Biosensors* **2022**, *12*, 721. [CrossRef] [PubMed]
6. Paliwal, N.; John, J. Lossy Mode Resonance (LMR) Based Fiber Optic Sensors: A Review. *IEEE Sens. J.* **2015**, *15*, 5361–5371. [CrossRef]
7. Naik, G.V.; Shalaev, V.M.; Boltasseva, A. Alternative Plasmonic Materials: Beyond Gold and Silver. *Adv. Mater.* **2013**, *25*, 3264–3294. [CrossRef]
8. Wang, H.; Prasad Sivan, V.; Mitchell, A.; Rosengarten, G.; Phelan, P.; Wang, L. Highly efficient selective metamaterial absorber for high-temperature solar thermal energy harvesting. *Sol. Energy Mater. Sol. Cells* **2015**, *137*, 235–242. [CrossRef]
9. Xu, Y.; Xuan, Y. Photon management of full-spectrum solar energy through integrated honeycomb/cone nanostructures. *Opt. Commun.* **2019**, *430*, 440–449. [CrossRef]
10. Bendelala, F.; Cheknane, A.; Hilal, H. Enhanced low-gap thermophotovoltaic cell efficiency for a wide temperature range based on a selective meta-material emitter. *Sol. Energy* **2018**, *174*, 1053–1057. [CrossRef]
11. Sakakibara, R.; Stelmakh, V.; Chan, W.R.; Ghebrebrhan, M.; Joannopoulos, J.D.; Soljacic, M.; Čelanović, I. Practical emitters for thermophotovoltaics: A review. *JPE* **2019**, *9*, 032713. [CrossRef]
12. Arya, S.; Mahajan, P. *Solar Cells: Types and Applications*; Springer Nature: Singapore, 2023. [CrossRef]
13. Bauer, T. *Thermophotovoltaics: Basic Principles and Critical Aspects of System Design*; Green Energy and Technology; Springer: Berlin/Heidelberg, Germany, 2011. [CrossRef]
14. Bermel, P.; Boriskina, S.V.; Yu, Z.; Joulain, K. Control of radiative processes for energy conversion and harvesting. *Opt. Express OE* **2015**, *23*, A1533–A1540. [CrossRef]
15. Green, M.A.; Emery, K.; Hishikawa, Y.; Warta, W.; Dunlop, E.D. Solar cell efficiency tables (version 40). *Prog. Photovolt. Res. Appl.* **2012**, *20*, 606–614. [CrossRef]
16. Mailoa, J.P.; Lee, M.; Peters, I.M.; Buonassisi, T.; Panchula, A.; Weiss, D.N. Energy-yield prediction for II–VI-based thin-film tandem solar cells. *Energy Environ. Sci.* **2016**, *9*, 2644–2653. [CrossRef]
17. Gamel, M.M.A.; Lee, H.J.; Rashid, W.E.S.W.A.; Ker, P.J.; Yau, L.K.; Hannan, M.A.; Jamaludin, M.Z. A Review on Thermophotovoltaic Cell and Its Applications in Energy Conversion: Issues and Recommendations. *Materials* **2021**, *14*, 4944. [CrossRef]
18. Lu, Q.; Zhou, X.; Krysa, A.; Marshall, A.; Carrington, P.; Tan, C.-H.; Krier, A. InAs thermophotovoltaic cells with high quantum efficiency for waste heat recovery applications below 1000 °C. *Sol. Energy Mater. Sol. Cells* **2018**, *179*, 334–338. [CrossRef]

19. Rühle, S. Tabulated values of the Shockley–Queisser limit for single junction solar cells. *Sol. Energy* **2016**, *130*, 139–147. [CrossRef]
20. Mamiyev, Z.; Balayeva, N.O. PbS nanostructures: A review of recent advances. *Mater. Today Sustain.* **2023**, *21*, 100305. [CrossRef]
21. Yu, P.; Wang, Z.M. (Eds.) *Quantum Dot Optoelectronic Devices*; Lecture Notes in Nanoscale Science and Technology; Springer International Publishing: Cham, Switzerland, 2020; Volume 27. [CrossRef]
22. Wang, H.; Kubo, T.; Nakazaki, J.; Segawa, H. Solution-Processed Short-Wave Infrared PbS Colloidal Quantum Dot/ZnO Nanowire Solar Cells Giving High Open-Circuit Voltage. *ACS Energy Lett.* **2017**, *2*, 2110–2117. [CrossRef]
23. Fu, Y.; Dinku, A.G.; Hara, Y.; Miller, C.W.; Vrouwenvelder, K.T.; Lopez, R. Modeling photovoltaic performance in periodic patterned colloidal quantum dot solar cells. *Opt. Express OE* **2015**, *23*, A779–A790. [CrossRef]
24. Burger, T.; Fan, D.; Lee, K.; Forrest, S.R.; Lenert, A. Thin-Film Architectures with High Spectral Selectivity for Thermophotovoltaic Cells. *ACS Photonics* **2018**, *5*, 2748–2754. [CrossRef]
25. Ni, Q.; Alshehri, H.; Yang, Y.; Ye, H.; Wang, L. Plasmonic light trapping for enhanced light absorption in film-coupled ultrathin metamaterial thermophotovoltaic cells. *Front. Energy* **2018**, *12*, 185–194. [CrossRef]
26. Saive, R. Light trapping in thin silicon solar cells: A review on fundamentals and technologies. *Prog. Photovolt. Res. Appl.* **2021**, *29*, 1125–1137. [CrossRef]
27. Cho, C.; Song, J.H.; Kim, C.; Jeong, S.; Lee, J.-Y. Broadband light trapping strategies for quantum-dot photovoltaic cells (>10%) and their issues with the measurement of photovoltaic characteristics. *Sci. Rep.* **2017**, *7*, 17393. [CrossRef] [PubMed]
28. Weiland, T. A discretization model for the solution of Maxwell's equations for six-component fields. *Arch. Elektron. Und Uebertragungstechnik* **1977**, *31*, 116–120.
29. Bendelala, F.; Cheknane, A.; Hilal, H.S.; Goumri-Said, S. Extremely Low-Loss Broadband Thermal Infrared Absorber Based on Tungsten Metamaterial. *J. Electron. Mater.* **2019**, *48*, 3304–3310. [CrossRef]
30. Li, H.H. Refractive Index of ZnS, ZnSe, and ZnTe and Its Wavelength and Temperature Derivatives. *J. Phys. Chem. Ref. Data* **1984**, *13*, 103–150. [CrossRef]
31. Yang, J.; Xu, C.; Qu, S.; Ma, H.; Wang, J.; Pang, Y. Optical transparent infrared high absorption metamaterial absorbers. *J. Adv. Dielect.* **2018**, *8*, 1850007. [CrossRef]
32. Bi, Y.; Bertran, A.; Gupta, S.; Ramiro, I.; Pradhan, S.; Christodoulou, S.; Majji, S.-N.; Akgul, M.Z.; Konstantatos, G. Solution processed infrared- and thermo-photovoltaics based on 0.7 eV bandgap PbS colloidal quantum dots. *Nanoscale* **2019**, *11*, 838–843. [CrossRef]
33. Grinolds, D.D.W.; Brown, P.R.; Harris, D.K.; Bulovic, V.; Bawendi, M.G. Quantum-Dot Size and Thin-Film Dielectric Constant: Precision Measurement and Disparity with Simple Models. Available online: https://pubs.acs.org/doi/pdf/10.1021/nl5024244 (accessed on 18 March 2023).
34. Moreels, I.; Lambert, K.; Smeets, D.; De Muynck, D.; Nollet, T.; Martins, J.C.; Vanhaecke, F.; Vantomme, A.; Delerue, C.; Allan, G.; et al. Size-Dependent Optical Properties of Colloidal PbS Quantum Dots. *ACS Nano* **2009**, *3*, 3023–3030. [CrossRef]
35. Rahimi, Z. *The Finite Integration Technique (FIT) and the Application in Lithography Simulations*; Friedrich-Alexander-Universitaet Erlangen-Nuernberg: Erlangen, Germany, 2011.
36. Ordal, M.A.; Bell, R.J.; Alexander, R.W.; Long, L.L.; Querry, M.R. Optical properties of fourteen metals in the infrared and far infrared: Al, Co, Cu, Au, Fe, Pb, Mo, Ni, Pd, Pt, Ag, Ti, V, and W. *Appl. Opt. AO* **1985**, *24*, 4493–4499. [CrossRef]
37. Bendelala, F.; Cheknane, A.; Benatallah, M.; Nunzi, J.-M. Extending the absorption band from infrared to ultraviolet using the ITO transition from reflection to transparence. *Eur. Phys. J. Appl. Phys.* **2021**, *96*, 10501. [CrossRef]
38. Kupresak, M.; Zheng, X.; Vandenbosch, G.A.E.; Moshchalkov, V.V. Benchmarking of software tools for the characterization of nanoparticles. *Opt. Express OE* **2017**, *25*, 26760–26780. [CrossRef]
39. Lee, Y.P.; Rhee, J.Y.; Yoo, Y.J.; Kim, K.W. *Metamaterials for Perfect Absorption*; Springer Series in Materials Science; Springer: Singapore, 2016; Volume 236. [CrossRef]
40. Silvester, P.P.; Ferrari, R.L. *Finite Elements for Electrical Engineers*; Cambridge University Press: Cambridge, UK, 1996. [CrossRef]
41. Zainud-Deen, S.H.; El-Shalaby, N.A.; Awadalla, K.H. Hemispherical DRA Antennas Mounted on or Embedded in Circular Cylindrical Surface forProducing Omnidirectional Radiation Pattern. *Int. J. Commun. Netw. Syst. Sci.* **2011**, *4*, 601–608. [CrossRef]
42. Fuentes, O.; Del Villar, I.; Dominguez, I.; Corres, J.M.; Matías, I.R. Simultaneous Generation of Surface Plasmon and Lossy Mode Resonances in the Same Planar Platform. *Sensors* **2022**, *22*, 1505. [CrossRef]
43. Zhang, W.-W.; Qi, H.; Yin, Y.-M.; Ren, Y.-T. Tailoring radiative properties of a complex trapezoidal grating solar absorber by coupling between SPP and multi-order MP for solar energy harvesting. *Opt. Commun.* **2021**, *479*, 126416. [CrossRef]
44. Wang, H.; Wang, L. Plasmonic light trapping in an ultrathin photovoltaic layer with film-coupled metamaterial structures. *AIP Adv.* **2015**, *5*, 027104. [CrossRef]
45. Miller, C.W.; Fu, Y.; Lopez, R. Enhancing energy absorption in quantum dot solar cells via periodic light-trapping microstructures. *J. Opt.* **2016**, *18*, 094002. [CrossRef]
46. Ganesan, A.A.; Houtepen, A.J.; Crisp, R.W. Quantum Dot Solar Cells: Small Beginnings Have Large Impacts. *Appl. Sci.* **2018**, *8*, 1867. [CrossRef]

47. Zhang, Z.M. *Nano/Microscale Heat Transfer*; Mechanical Engineering Series; Springer International Publishing: Cham, Switzerland, 2020. [CrossRef]
48. Ding, C.; Wang, D.; Liu, D.; Li, H.; Li, Y.; Hayase, S.; Sogabe, T.; Masuda, T.; Zhou, Y.; Yao, Y.; et al. Over 15% Efficiency PbS Quantum-Dot Solar Cells by Synergistic Effects of Three Interface Engineering: Reducing Nonradiative Recombination and Balancing Charge Carrier Extraction. *Adv. Energy Mater.* **2022**, *12*, 2201676. [CrossRef]